Full Length Article

Tribological behaviour of AZ31 magnesium alloy reinforced by bimodal size B$_4$C after precipitation hardening

Seyed Kiomars Moheimani[a,b], Azadeh Keshtgar[c], Saeed Khademzadeh[d], Morteza Tayebi[e,*], Ali Rajaee[f], Abdollah Saboori[g]

[a] Advanced Materials Research Center, Department of Materials Engineering, Najafabad Branch, Islamic Azad University, Najafabad, Iran
[b] Department of Research and Development, Nejat Darya Company, Boushehr, Iran
[c] Center for Risk and Reliability, University of Maryland, College Park, MD 20742, United States
[d] Department of Industrial Engineering, University of Padova, 35131 Padova, Italy
[e] Young Researchers and Elites Club, Science and Research Branch, Islamic Azad University, Tehran, Iran
[f] Department of Materials and Polymer Engineering, Hakim Sabzevari University, Sabzevar, Iran
[g] Integrated Additive Manufacturing Center (IAM), Department of Management and Production Engineering (DIGEP), Politecnico di Torino, Corso Duca Degli Abruzzi, 24, 10129, Torino, Italy

Abstract

This study investigated dry sliding wear properties of AZ31 magnesium alloy and B$_4$C-reinforced AZ31 composites containing 5, 10, and 20 wt.% B$_4$C with bimodal sizes under different loadings (10–80 N) at various sliding speeds (0.1–1 m/s) via the pin-on-disc configuration. Microhardness evaluations showed that when the distribution of B$_4$C particles was uniform the hardness of the composites increased by enhancing the reinforcement content. The unreinforced alloy and the composite samples were examined to determine the wear mechanism maps and identify the dominant wear mechanisms in each wear condition and reinforcement content. For this purpose, wear rates and friction coefficients were recorded during the wear tests and worn surfaces were characterized by scanning electron microscopy and energy dispersive X-ray spectrometry analyses. The determined wear mechanisms were abrasion, oxidation, delamination, adhesion, and plastic deformation as a result of thermal softening and melting. The wear evaluations revealed that the composites containing 5 and 10 wt.% B$_4$C had a significantly higher wear resistance in all the conditions. However, 20 wt.% B$_4$C/AZ31 composite had a lower resistance at high sliding speeds (0.5–1 m/s) and high loadings (40–80 N) in comparison with the unreinforced alloy. The highest wear resistance was obtained at high sliding speeds and low loadings with the domination of oxidative wear.

1. Introduction

Currently, to meet lightweight standards, the development of high strength-to-weight ratio materials is inevitable, which plays a significant role in energy saving for structural applications. Mg alloys can be an alternative to the conventional alloys used for gears, bearings, cylinder bores, and pistons due to their unique properties, namely high specific ductility, low density, and great shock absorption [1–3]. Nevertheless, low mechanical properties of Mg alloys, especially low wear resistance, can be a restriction for being used in industrial applications [4], which is critical in automotive and aircraft engine components [5,6]. Compositing is an efficient method to develop the mechanical and wear properties of Mg alloys. In the meantime, their reinforcement selection is the most important factor in the composite preparation process along with

* Corresponding author.
E-mail addresses: morteza.tayebi@srbiau.ac.ir, m.tayebi@stu.sku.ac.ir (M. Tayebi).

the evolution of the microstructure and reinforcement distribution in the matrix [7,8]. However, tribological properties of the composites are also highly dependant on the matrix and reinforcement materials (size, shape, content, and distributions), experimental conditions (loading, environment, sliding speed, and sliding distance) and surficial conditions (e.g. roughness and hardness) [5,9]. The description of the aforementioned parameters is brought in details in a previous study [5].

Particle-reinforced metal-matrix composites (MMCs) display great mechanical and wear properties compared to unreinforced metals due to the existence of hard reinforcement particles in them, protecting the material from continuous abrasion during tribo-contacts [9–11]. Results of an earlier investigation have shown that although the addition of the SiC microparticles to Mg matrixes leads to improved mechanical properties, homogenous distribution is not attained in the matrix. Different factors affect the wear resistance of MMCs, amongst which some are well-known. For instance, particle size has been stated to have conflicting results. A few studies have claimed that fine-sized particles enhance wear resistance by increasing the composite strength. Such reports concern mechanisms such as dislocation strengthening, Orowan strengthening, and grain refinement strengthening. An improvement in the friction can also be seen as a result of more particle/counterface contacts. Other studies have proposed that large reinforcement sizes can increase the wear resistance through deep embedment in the matrix and improve load-bearing capacity [12]. Based on the mentioned findings, it can be concluded that both fine and coarse particles can have positive effects on the improvement of the friction and wear resistance of MMCs. Thus, composites reinforced by bimodal size particles are expected to have a combination of both particle types. Fine (submicron-scale) and coarse particles (micron-scale) in the matrixes assist grain refinement by stimulating dynamic recrystallization and nucleation, and grain boundary pinning during the mechanical processes, respectively. Thus significant strengthening has been achieved [13].

An increase in the particle content results in the development of the wear resistance of MMCs by inter-particle spacing on the tribological properties of the composites [1]. Micro/nano-scaled particles of SiC [7,8,14,15], B_4C [16–18], Al_2O_3 [5,10], and CNT [19] are typically employed as the reinforcement particles which improve the hardness, strength and elastic modulus of the composites [1,2]. Amongst them, B_4C is a more suitable alternative for the improvement of MMCs properties such as high melting point, high thermal stability, excellent abrasion resistance, high hardness, great neutron absorption, and low density [16,17].

In addition, B_4C density is 2.52 g/cm^3, whereas Mg density is 1.74 g/cm^3. Hence, B_4C/Mg composites are considered as lightweight materials with density values of around 2 g/cm^3 even if 50 vol.% B_4C particles are introduced [20]. It is worth noting that B_4C/Mg composites containing a high volume fraction of ceramic particles show excellent wear resistance that can have a great potential for aerospace applications.

Several methods have been employed for the preparation of Mg-matrix composites, including powder metallurgy [21,22], pressureless infiltration [23], stir casting, and squeeze casting [1,2]. Powder metallurgy can offer homogeneous distribution of particles in the matrix, resulting in a low reaction of the matrix and reinforcement [16]. Recently, researchers have tried many other techniques for uniform distribution of particles, including high energy ball milling, friction stir processing, squeeze casting, spread dispersion method, and spray deposition. Amongst these techniques, stir casting has attracted great attention due to its simplicity, uniform distribution of reinforcement, and ability to prepare complex-shaped products. Only few investigations were carried out on the preparation of B_4C/Mg composites using stir casting [24,25]. But, several studies have been carried out on the preparation of B_4C/Mg composites via other techniques [20,26–29]. For instance, Ghasali et al. [30] fabricated 5 wt.% B_4C/Mg composites by spark plasma sintering process and investigated the hardness and bending strength of the composites. They stated that although the strength and hardness of the prepared composites were improved compared with those fabricated via conventional methods, brittle phases of MgB_2 and Mg_2C_3 were formed in the microstructure. Additionally, Jiang et al. [28] prepared B_4C/Mg composites by powder metallurgy and evaluated their wear behaviour. They reported that the wear properties of the reinforced samples were improved, respecting the unreinforced samples. However, they did not examine extensive conditions to obtain detailed information on the wear mechanisms.

There are numerous investigations in the literature on the sliding wear behaviour of the dendritic Mg alloys and their composites. For instance, Somekawa et al. [31] evaluated the wear behaviour and the microstructural evolution of commercially pure Mg and Mg–Y alloys during the wear tests. Their findings revealed that the wear rate of Mg alloys was superior to that of pure one, which was related to the formation of $\{10\bar{1}2\}$ twinning.

Surface treatment techniques such as physical vapour deposition and plasma electrolytic oxidation have been frequently used to enhance the wear properties of Mg alloys and composites [32]. The effect of the addition of oxide and carbide-based reinforcements on the wear behaviour of Mg materials was also investigated [33]. Chen et al. [34] reported two wear regimes for the as-cast AZ91 Mg alloy; the severe wear, in which severe plastic deformation and melt wear were the dominant mechanisms, and the mild wear regime, which was dominated by oxidation and delamination wear mechanisms. By studying the temperature of the contact surface of each material, they found that the equilibrium temperature could determine the transition between the regimes. On the contrary, Wang et al. [35] demonstrated that the mild wear regime occurred during low loadings, irrespective of the test temperature. This can be attributed to the formation of a thick layer consisting of Mg and $MgAl_2O_4$, known as the mechanical mixing layer (MML). Taltavull et al. [36] constructed a wear map for AM60B Mg alloy at different loads (10–250 N) and various sliding speeds of 0–1 m/s. Results showed that at

S.K. Moheimani, A. Keshtgar, S. Khademzadeh et al.

Table 1
Chemical composition of the AZ31 Mg alloy.

Element	Al	Zn	Ni	Fe	Mn	Cu	Mg
wt%	3	1	0.03	0.05	0.2	0.03	Bal.

lower loadings, the dominant wear mechanisms were oxidation, delamination, and adhesion, whereas, at higher loadings, the dominant wear mechanism was altered by severe plastic deformation. Moreover, the wear properties of AZ91 alloy were evaluated by Zafari et al. [37]. They determined the severe plastic deformation wear regimes for AZ91 alloy at different loadings. Furthermore, their study demonstrated that the sample temperature was effective in the determination of the wear mechanism. In a similar vein, Lim et al. [33] investigated the wear behaviour of SiC-reinforced AZ91 alloy during the dry sliding wear test. It was reported that the addition of the reinforcement particles was only effective at low loadings. Habibnejad et al. [38] also compared the tribological behaviours of commercially pure Mg and AZ31 composites reinforced by Al_2O_3 nanoparticles. It was shown that the wear rate declined with increasing the reinforcement content. The improved wear behaviour was related to the composite strengthening mechanisms such as mismatch hardening mechanism and the load-bearing ability of the hard ceramic particles.

To the best of the authors' knowledge, before the publication date of the present paper, no comprehensive study in the literature has been conducted concerning the effect of microstructure on the wear properties of B_4C/Mg composites prepared by stir casting in details. However, the field of wear behaviour of B_4C/Mg composites still requires detailed investigation. For this reason, the current study focused on the wear properties of B_4C/Mg composite samples prepared by stir casting. In addition, the dominant wear mechanisms were also comparatively evaluated for both the unreinforced Mg and B_4C-reinforced Mg composites.

2. Materials and method

2.1. Materials

AZ31 magnesium alloy (Shandong Hongtai Science and Technology Co., Ltd., China) was selected as the $B_4C/AZ31$ composites matrix, and its chemical composition is shown in Table 1. A mixture of bimodal B_4C particles (Merck Co., Germany) with average diameters of 1 and 50 μm and the ratio of 1:5 was added as the reinforcement.

2.2. Sample preparation

The stir casting method was employed for the $B_4C/AZ31$ composites preparation, as demonstrated in Fig. 1. To obtain a uniform heat distribution, the furnace temperature was increased gradually from 100 to 780 °C. A gaseous mixture of carbon dioxide (CO_2) and sulfur fluoride (SF_6) was inserted into the furnace at 300 °C to avoid burning, while argon gas
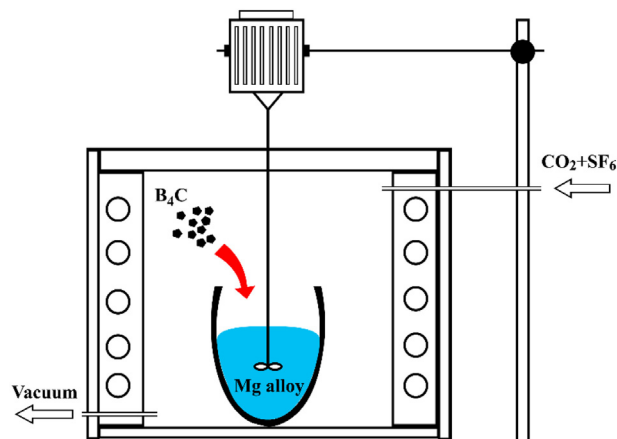

Fig. 1. Schematic of the stir casting method employed for preparation of $B_4C/AZ31$ composite samples.

was injected at 600 °C to prevent oxidation. After stabilization at 780 °C for 20 min, the B_4C particles were preheated at 200 °C and added to the melt via vortex method. For gaining a uniform distribution of B_4C particles in the matrix, the melt was stirred at 350 rpm for 8 min. Finally, the melt was poured into a steel mould. Four types of composites with 0, 5, 10, and 20 wt.% B_4C contents were prepared. The samples were heated at 400 °C in an atmosphere-controlled furnace for 10 h to homogenize the chemical composition; then, they were quenched in water and aged artificially at 175 °C for 10 h.

2.3. Density

The practical density was measured via the Archimedes principle. The theoretical density of the composite samples was determined by dividing the sample mass by its volume. The average theoretical density of each sample was calculated as a result. The porosity of the samples was measured using Eq. (1) [8].

$$P = \left[1 - \frac{\rho_a}{\rho_t}\right] \times 100 \qquad (1)$$

where ρ_a and ρ_t are the skeletal and apparent density values of the samples, respectively. Four samples of each composite were tested, and the average value was reported as the final result.

2.4. Hardness

The microhardness of the samples was measured using a Vickers microhardness testing machine (Leitz, England) equipped with a diamond indenter. A 300-N load was applied with a dwell time of 20 s. Five replicate measurements were carried out, and the average value was reported as the microhardness.
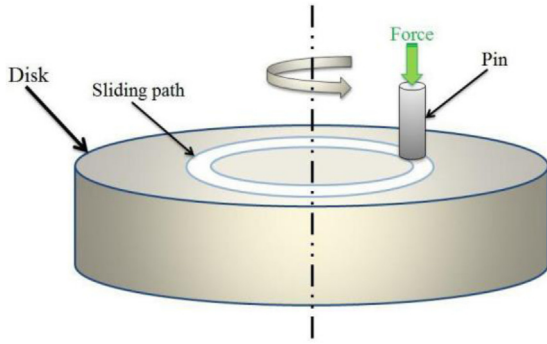
Fig. 2. Schematic of pin-on-disk configuration used for the sliding wear tests.

2.5. Wear test

Dry sliding wear tests were carried out using an AISI 52,100 steel pin with a hardness of 45 HRC and pin-on-disk configuration at ambient temperature, as shown in Fig. 2. Samples with dimensions of 35 mm $\varphi \times$ 5 mm were utilized for the tests, and the steel pin had a 5 mm effective diameter. All tests were performed at the loadings of 10, 20, 40, and 80 N, the sliding speeds of 0.1, 0.3, 0.7, and 1 m/s, and the sliding distance of 1000 m. This sliding distance was prolonged to 1000 m to ensure that the steady-state regime was reached. The surface of the samples was cleaned and degreased by acetone in an ultrasonic bath for 5 min. The weight loss was determined by measuring the sample weight before and after each test using a photoelectric weight balance. The volume loss was also calculated by dividing the weight loss by the density of each sample. The wear rates of the samples were assessed by Archard's law which can be expressed as Eq. (2) [39].

$$\frac{V}{L} = K\left(\frac{F}{H}\right) = kF \qquad (2)$$

where L is the sliding distance, V is the wear volume loss, F is the applied load, k is the specific wear rate, H is the hardness, and K is the Archard's constant. The average friction coefficient was also calculated for the wear distance. The applied tangential force on the holder was determined, and the coefficient of friction (COF) was calculated based on a function of the applied load. The perpendicular position of the holder was monitored to observe the displacement caused by the material removal during the wear test. Three replicates of each sample were tested, and the average COF value was reported as the final result.

2.6. Characterizations

Samples were grounded using 200, 400, 800, 1000, and 2500-grit sandpapers, and then they were polished by alumina suspension to obtain a mirror-like surface. The samples were etched by a solution of 10 mL nitric acid, 10 mL deionized water, and 75 mL ethanol for 20 s. The microstructure of the samples was studied using scanning electron microscopy (SEM) Philips (model PW1800, Netherlands) equipped with
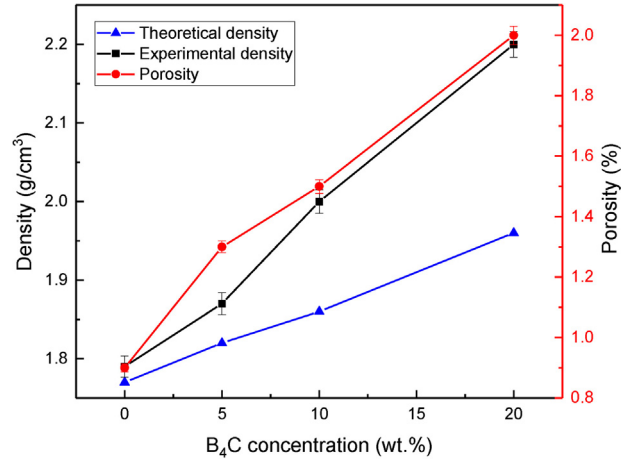

Fig. 3. Density and porosity of the samples containing different B_4C contents.

energy-dispersive X-ray spectroscopy (EDS). The grain size was calculated by the linear intercept method based on three metallography images with different magnifications to improve the precision of the data.

3. Results and discussion

3.1. Density

Fig. 3 demonstrates variations of density and porosity for the samples. An increase was evident in the bulk density by increasing B_4C content, which implied the strong bonding between ceramic particles and the alloy matrix. This increase was also attributed to the higher density of B_4C compared to that of the matrix. The porosity of composite samples remained almost constant by increasing B_4C content up to 10 wt.%. This trend could be related to the uniform distribution of the B_4C particles in the matrix caused by the shearing of the melt during the stirring process [40]. It can be concluded that the formation of an efficient bonding between the particles and the matrix, proper wettability of the particles by the melt, and suitable reinforcement distribution led to a reduction in the porosity. According to Fig. 4, the microstructural characterizations confirmed that a proper adhesion between the ceramic particles and the matrix was achieved due to the good wettability between them. It was also observed that sample 20 wt.% B_4C/AZ31 had a higher porosity. Uniform dispersion of B_4C in the matrix is a major benefit in the manufacturing of MMCs. A recent investigation in this field has reported that the agglomeration phenomenon can become dominant and exacerbate the porosity for composites containing ceramic particle higher than 10 wt.% [41]. Although all pores cannot be eliminated, they can be efficiently controlled by adjusting the casting parameters, namely stirring conditions, pouring method, and casting atmosphere neutralization [40].
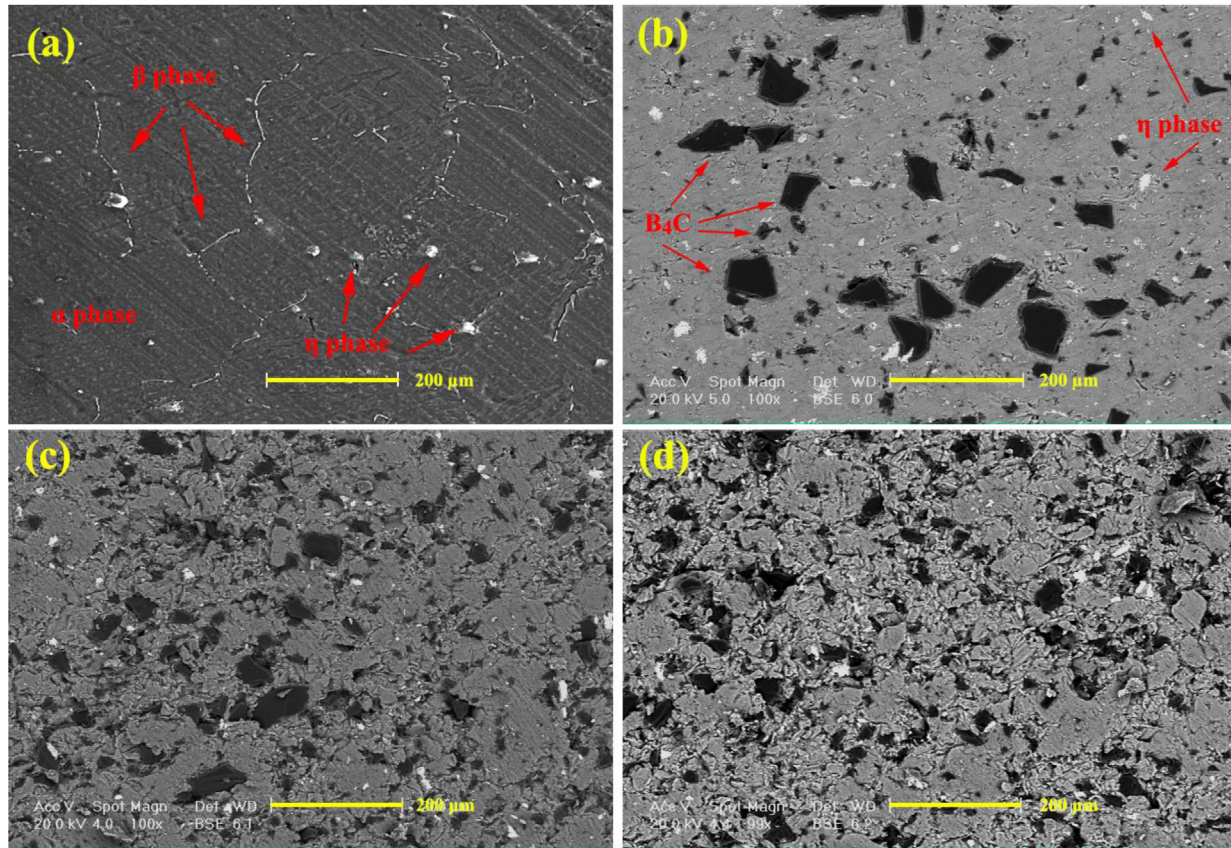
Fig. 4. SEM micrographs of the as-cast samples with different B$_4$C contents: (a) unreinforced alloy, (b) 5% B$_4$C/AZ31, (c) 10% B$_4$C/AZ31, and (d) 20% B$_4$C/AZ31.
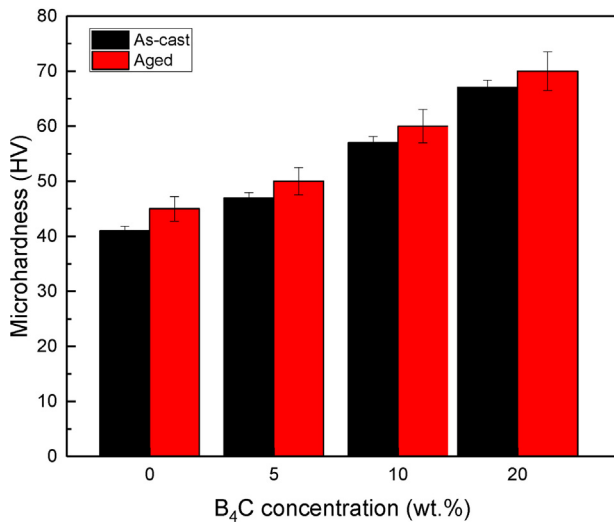

Fig. 5. Microhardness variation of the samples containing different B$_4$C concentrations before and after the ageing treatment.

3.2. Microhardness measurement

The microhardness of the samples with various weight percentages of B$_4$C is shown in Fig. 5. As can be seen, the microhardness of the samples was increased by elevating the B$_4$C content. The increase in the hardness was attributed to the presence of B$_4$C particles due to three possible strengthening mechanisms. First, an increase in the strength was due to the effective load transfer from the matrix to the reinforcement, in which the effect of microparticles is more noticeable to that of submicron particles. Second, an increase in the strength according to the Hall-Patch effect, which can be achieved through the grain refinement, resulted from the presence of particles. Moreover, by increasing the number of particles, the inter-particle spacing is reduced. Accordingly, the elastically-deformed regions around the ceramic particles are overlapped, providing the required activation energy for the grain refinement. During this mechanism, the presence of submicron particles is more effective in attaining a uniform distribution and reduction of the inter-particle spacing (Fig. 4). This aim can be achieved by the bimodal distribution of the B$_4$C particles. The bimodal distribution prevents the localized deformation of the matrix surface during the test and refines matrix grain size [42]. Localized deformation of composites and showed that deformation in the composites with high volume fraction of reinforcement was highly localized, which is due to clustering and agglomeration. They reported that the slip lines initiated in regions containing many clusters of SiC particles. Then, the slip lines spread from one cluster region to another, while the deformation remains almost zero in other samples. Moreover, in general, it should be said that by increasing the volume fraction of reinforcement, the strength of the material increased, and it is less prone to plastic deformation. To

S.K. Moheimani, A. Keshtgar, S. Khademzadeh et al. *Journal of Magnesium and Alloys xxx (xxxx) xxx*

clarify the reason for the initiation of the plastic deformation in the clustered regions, deformation compatibility of inhomogeneous (clustering) distribution of reinforcement particles should be considered. The reason can be related to the higher stiffness of the clusters, which bear higher loading than the rest of the matrix to satisfy the deformation compatibility. On the other hand, the local volume fraction is higher in the clusters; thus for the same extent of deformation, more slip systems must be activated in the matrix. When the effective plastic strain diverges at various locations of the matrix, the total applied strain reaches zero, indicating the existence of a large gradient of plastic deformation in the matrix, which is due to primary residual thermal stresses [43]. Third, an increase in the hardness can be related to the presence of hard B_4C particles in the soft Mg matrix. The difference in the thermal expansion coefficients of the reinforcement particles and the matrix can lead to the formation of mismatch dislocations that improve the strength of the matrix up to the plastic level and increase the hardness [16,44]. In this mechanism, the presence of both particle types can also be effective due to the increase in the dislocation density in the matrix [13]. Here, the density increase contributed to the increase in the hardness. By increasing the reinforcement content up to 20 wt.%, the hardness value was increased up to 68.50 HV. Although the hardness was improved by rising the B_4C content for all the samples, the increasing rate of the hardness was lowered when the reinforcement content increased from 10 to 20 wt.%. The reduction in the hardness rate was credited to the agglomeration of B_4C particles, which led to a decrease in densification and hardness deterioration [14]. In this study, the reduction in the hardness rate due to the agglomeration was low, indicating the successful compensation of the mechanisms of grain refinement, mismatch dislocations, and load transfer for hardness. It was revealed that the microhardness of the aged composite samples was slightly higher than those of as-cast ones, which might be related to two factors; first, activation of the Orowan mechanism due to the presence of precipitations acting as barriers to the dislocation movement, and second dynamic recrystallization and grain refining phenomena during the ageing process [45]. It has been reported that the existence of the reinforcement in the matrix assists the precipitation nucleation at the early stages of dynamic recrystallization and declines the average grain size of the matrix [46]. Overall, the most common recrystallization mechanism in Mg alloys is continuous dynamic recrystallization, which declines the grain size during ageing treatment [47]. This phenomenon also results in increase in the precipitation content, which are dissolved during solid solution, re-dispersed along the grain boundaries, and prevent the grain coarsening, leading to improvement of the mechanical properties via dynamic Hall-Petch effect [48].

3.3. Microstructure evaluation

Fig. 4a demonstrates the microstructure of the unreinforced AZ31 alloy. Dark and bright regions in the figure represent primary α-phase grains and β-phases, respectively. As de-
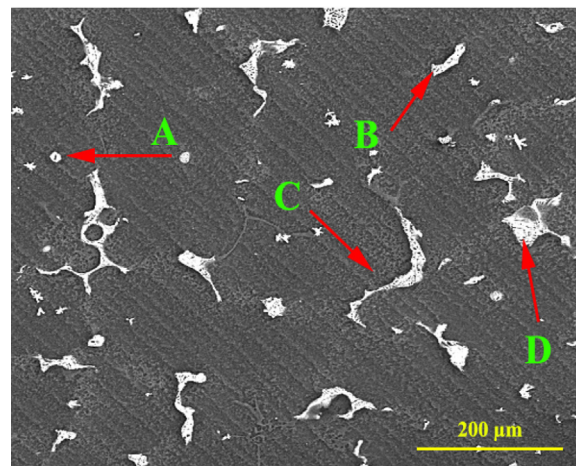

Fig. 6. SEM micrograph of aged unreinforced alloy indicating the presence of the precipitations with dendritic morphology.

scribed in earlier studies, the β-phase locating at the grain boundaries consists of $Mg_{17}Al_{12}$ compound [49,50]. Moreover, η-phase particles with Al_8Mn_5 composition are present in both inter-dendritic regions and α-phase grains, which is due to the presence of 0.2 wt.% Mn. Since mechanical stirring has been utilized, this phase formed a continuous network through the microstructure [49,51]. As demonstrated in Fig. 4b-d, a bimodal distribution of B_4C particles is evident in the samples, which are mostly distributed in the α-phase. Figs 4c and d display the effect of B_4C content on the average grain size of the B_4C/AZ31 composites. It is noticeable that the addition of B_4C causes a decline in the grain size to 5 μm. In fact, the grain size was reduced by enhancing the B_4C content. The grain refinement is ascribed to the distribution of B_4C particles in the microstructure, pinning the grain boundaries and resulting in heterogeneous nucleation of precipitations. Moreover, it is evident that the grains around the B_4C microparticles are finer than those around the submicron B_4C particles. It can be deduced that B_4C microparticles were more efficient in grain refinement in comparison to the submicron B_4C particles. In addition, it was observed that B_4C microparticles were mainly distributed in the grain boundaries, while B_4C nanoparticles were both distributed in the grain boundaries and inside the grains.

Fig. 6 and 7 show the SEM micrographs of the unreinforced alloy and 10 wt.% B_4C/AZ31 composite samples after ageing treatment, respectively. According to Fig. 6, the microstructure of the unreinforced AZ31 alloy mostly consists of MgZn (spot A in Fig. 6), Mg_2Al_3 (B in Fig. 6), $Mg_{17}Al_{12}$ (C in Fig. 6), and Al_4Mn (D in Fig. 6) compounds, which was approved by EDS analysis. In the present research, the compounds were uniformly distributed in the samples. The η-phase precipitations were formed continuously and discontinuously at the grain boundaries. The precipitations marked in Fig. 6 had a dendritic morphology. The buildup of the solute phases and high temperature of the interface could cause conditions in which the melt was super-cooled in the solidification front. During these conditions, the interface became
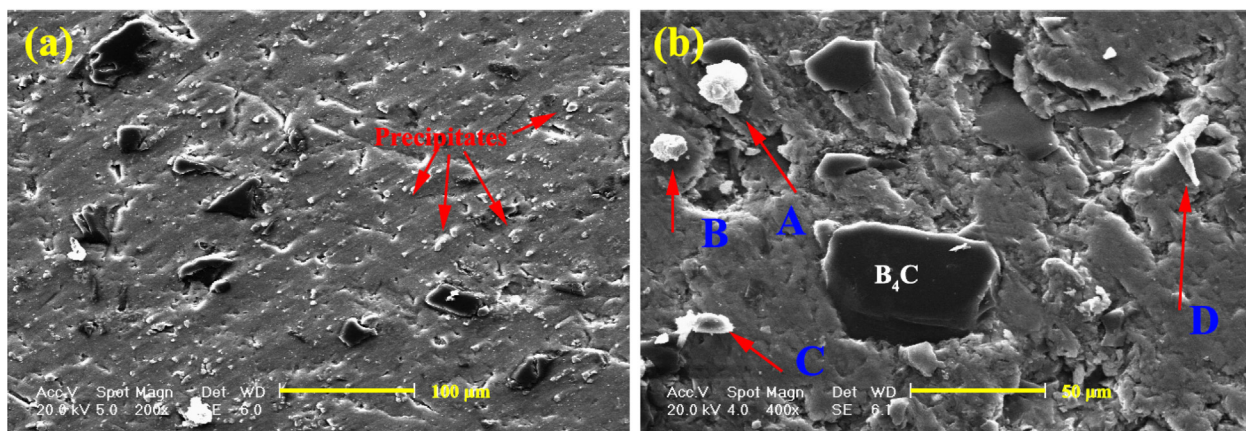
Fig. 7. SEM micrographs of the aged sample 10% B$_4$C/AZ31 with different magnifications.

unstable that resulted in dendritic solidification. Because of interface instability, the dendrites tended to branch. The precipitations were concentrated by the addition of B$_4$C particles at the grain boundaries. For the as-cast 20 wt.% B$_4$C/AZ31 composite sample, the Mg$_{17}$Al$_{12}$ compound was diffused or dissolved in the matrix, which left behind shallow pores at the grain boundaries. These pores were also noticeable in sample 20 wt.% B$_4$C/AZ3 approving the results discussed in the porosity section.

By comparing Figs. 4 and 7, it can be said that ageing affects the diffusion and phase-generation processes in the matrix. It is evident that the β-Mg$_{17}$Al$_{12}$ phase was entirely dissolved, and instead, a granular intermetallic phase was formed close to the grains and at grain boundaries. The improvement in the mechanical strength was generally caused by the formation of thermodynamically stable phases, grain refinement, and diffusion of β-Mg$_{17}$Al$_{12}$. EDS elemental analysis of A and B regions supported the presence of Mg$_2$Al$_3$ and Al$_4$Mn$_3$ compounds.

3.4. Wear rate

Contour plots of volumetric wear rate were developed for aged samples to facilitate the determination of sliding speed and applied load parameters (Fig. 8). The data uncertainty was represented by the error bars, which was lower than 3%. Besides, by plotting the contour maps, the zones where B$_4$C particles improved the wear behaviour of the composites were easily determined. B$_4$C particles could pin the grain boundaries and prevent the grain boundary sliding. The reinforcement particles acted as a bonding agent in the matrix and improved the wear resistance. The wear behaviour of materials resulted from different parameters, including grain refinement, porosity, strength, and hardness. The reduction in weight loss was related to the addition of B$_4$C particles, which enhanced the strength and hardness of the composite samples. At all sliding speeds, a similar trend was detected (Fig. 8a-c). With increasing the load for both unreinforced and composite samples, the volumetric wear rate increased that could be predictable by Archard's law; however, decreases in the wear

rate were detected under certain conditions. According to Archard's law, the weight and volumetric loss for all samples declined with increasing the hardness (Figs. 4 and 2). The wear rate of the composite containing 20 wt% B$_4$C differed slightly with respect to other samples. The composite samples showed lower hardness through the initial stage of sliding wear compared with the subsequent stages because after a certain sliding distance, the composites were subjected to strain hardening under the applied load during the continuous sliding [52]. As can be seen, no rapid change in the wear behaviour is observed in the graph. The graphs of volumetric wear rate after the dry sliding test as a function of B$_4$C content are shown in Fig. 8b-d. Their trends were similar to that of dry sliding tests showing the reduction of wear rate during the tests. This phenomenon was related to surface plastic deformation. Furthermore, it was observed that regardless of the test speed, the wear rate of the sample 20 wt.% B$_4$C/AZ31 was higher than that of the unreinforced sample under elevated loadings. Arrows on the contour maps of the wear rates show the zones where the reinforcement particles deteriorate the wear resistance (Fig. 8b and c). The most significant dissimilarity was seen over the speed range of 0.6–1 m/s (Fig. 8d). Hence, the presence of B$_4$C particles deteriorated the wear resistance of AZ31 alloy at elevated loadings. However, under low loadings (10–40 N), B$_4$C reinforcement enhanced the wear resistance in comparison to the unreinforced AZ31 alloy at nearly all speeds (Fig. 8a and d). Over the speed range of 0.1–0.5 m/s, the increase in the B$_4$C content of the composite samples appeared to be beneficial to the wear resistance. For example, the wear rates of samples 10 wt.% B$_4$C/AZ31 and 5 wt.% B$_4$C/AZ31 reduced by ~30% and ~10% compared to unreinforced alloy, respectively. Nonetheless, under lower loadings, the dissimilarity of the wear rates was not significant.

The maximum wear rate was attained under high loadings for all sliding speeds, but it decreased when the sliding speed was decreased for composite samples. It was deduced that the dependence of the wear rate on the sliding speed was more notable under lower loadings.
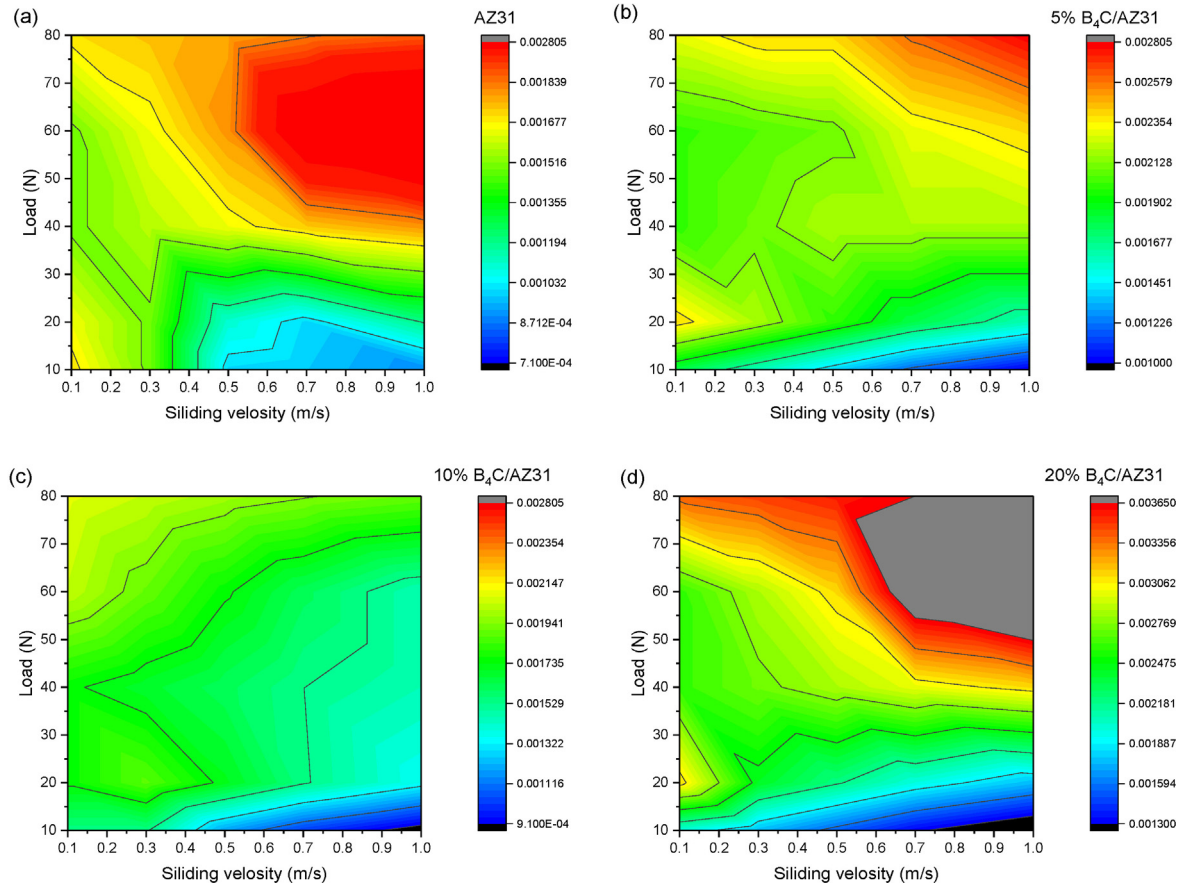
Fig. 8. Contour plots of volumetric wear rates (mm^3/Nm) of the samples with different B$_4$C contents: (a) unreinforced alloy, (b) 5% B$_4$C/AZ31, (c) 10% B$_4$C/AZ31, and (d) 20% B$_4$C/AZ31.

3.5. Friction coefficient

Graphs of friction coefficient as a function of sliding speed are shown in Fig. 9. It was found that the friction coefficient of the unreinforced alloy was much lower than that of the composite samples. Additionally, sample 20 wt.% B$_4$C/AZ31 had the highest friction coefficient. All the friction coefficients were lower than 0.75, and in most cases, they were below 0.5. The friction coefficient was unsteady under low loadings up to 40 and 20 N for the unreinforced and the composite samples, respectively. On the other side, in the mentioned loading ranges, by elevating the applied load, the coefficient was slightly decreased, stabilized, and almost independent of the sliding speed. Similarly, the composite samples with higher reinforcement contents showed higher friction coefficients. It can be concluded that different wear mechanisms were dominant for different test conditions and various reinforcement contents. The composites containing high reinforcement contents showed a more stable friction coefficient, which was attributed to the wear behaviour of B$_4$C particles. However, the decrease in the friction coefficient of aged composite samples was due to the formation of the Mg$_{12}$Al$_{17}$ phase that ameliorates the wear resistance. Indeed less ploughing grooves cased impede the wear process, which decreases in friction coefficient [53]. Regarding Ramezani and Ripin's friction model

[54], the coefficient of friction can be determined via calculating F$_f$/F$_n$. The friction force was directly associated with the friction coefficient under similar loading conditions. Consequently, it could be concluded that wear resistance was related to the friction coefficient.

3.6. Worn surface

Fig. 10a and b reveal the worn surfaces of the unreinforced and 10 wt.% B$_4$C/AZ31 samples at a speed of 0.1 m/s, and loading of 10 N. In both images, grooves parallel to the sliding direction are evident, which is a characteristic of the abrasive wear. This mechanism was detected at low loadings and all sliding distances for all samples. These grooves were normally caused by the hard counterface that has ploughed the soft surface of the samples. The material surface was removed during this mechanism, and the mentioned grooves were formed at the surface. A similar case can be observed for samples containing 5 and 20 wt.% B$_4$C. The abrasion mechanism was more evident in the unreinforced sample so that the formed grooves were more severe than those of the composite samples (Fig. 10b). In fact, by increasing the B$_4$C content, the abrasion mechanism was delayed.

Fig. 10c and d show the worn surfaces of the unreinforced and 10 wt.% B$_4$C/AZ31 samples at the speed of 1 m/s, and
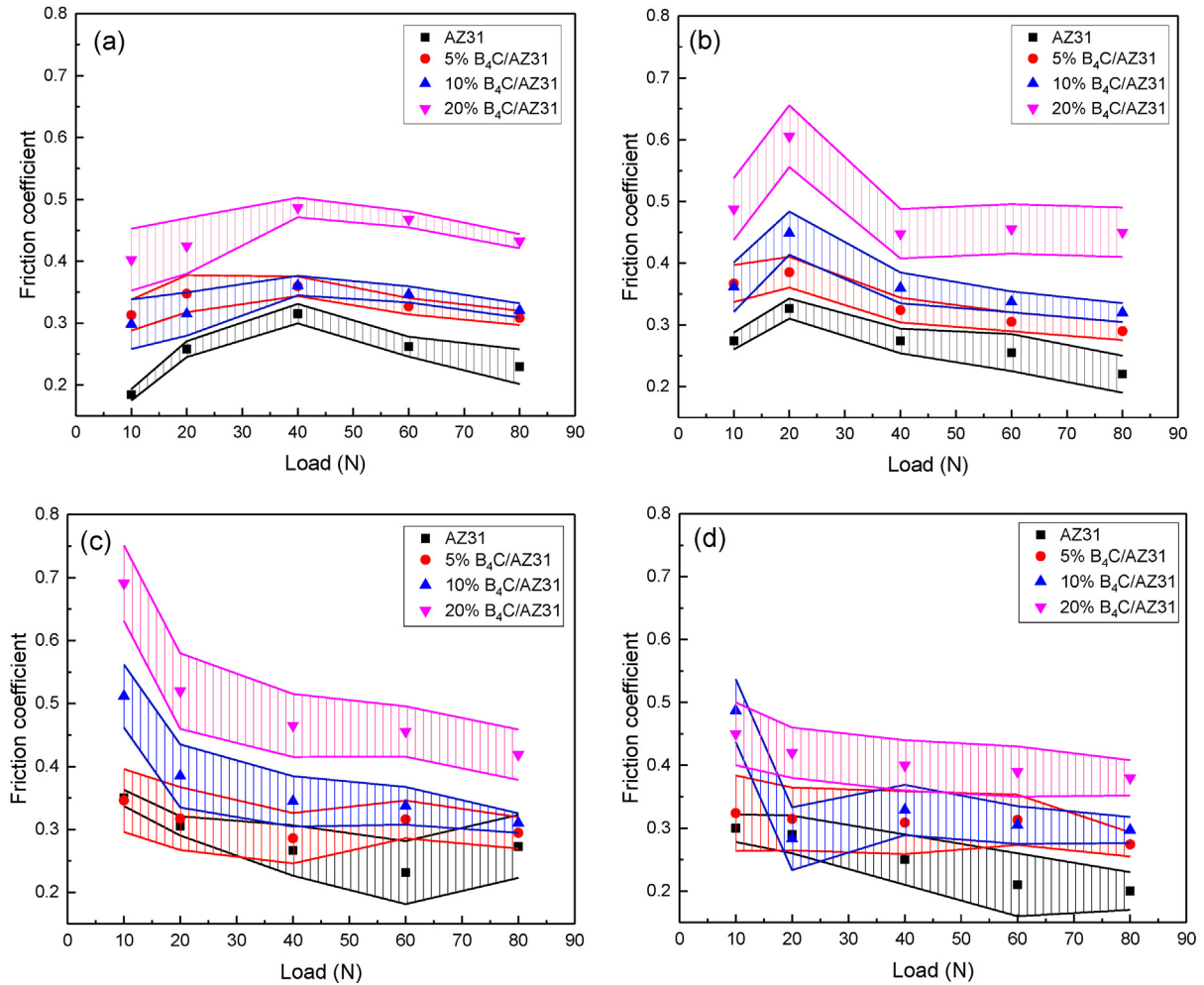
Fig. 9. Friction coefficient variations vs. loading for samples with different B$_4$C contents at: (a) 0.1 m/s, (b) 0.3 m/s, (c) 0.7 m/s, and (d) 1 m/s.

load of 10 N. As can be seen, a thin layer of oxide is formed almost everywhere on the surface of the unreinforced sample. The presence of the compact oxide layer on the surface leads to the improvement of the wear-resistant. The oxygen concentration of the abraded surfaces confirms the domination of the oxidative wear (Fig. 10I). In addition, SEM and EDS analyses of the worn surface approved the occurrence of severe oxidization. This phenomenon comes back to the generated heat during the sliding that led to the surface oxidation. Thereafter, the wear occurred due to the elimination of the oxidized fragments (Fig. 10e). In some conditions, the detached oxide particles filled the voids, mixed with the surface composition, and formed a protective oxide layer during the wear test, known as MML [55,56]. The formation of this oxide layer during the wear test prevented the contact of the pin and sample, and as a consequence, the wear rates decrease. The MML reduced the friction coefficient, which is evident in Fig. 9d. In previous works, it is reported that Mg alloys are susceptible to oxidation, and this tendency affects their wear rates [40]. In this research, during continuous sliding, the brittle layer composing of MgO and/or Mg$_2$Al$_2$O$_4$ was fractured and formed fragments and a protective oxide layer on the surface of the alloy, which prevented the sliding surfaces from metal-to-metal contact during sliding. By comparing the wear rates of the unreinforced alloy and composite samples at the sliding speed of 1 m/s and loading of 60 and 80 N, it was revealed that the composite samples had a lower value. For composite samples under these conditions, oxidative wear was the dominant mechanism, and the formed oxide layer lowered the wear rate. Besides, this phenomenon occurred for the unreinforced alloy, which had a low wear rate. This could be related to two factors; (i) removal of the formed oxide layer of the unreinforced alloy due to low strength, (ii) exposure of a new surface to the wear and oxidation. In fact, oxidation of the new surface increases the wear rate. Moreover, the difference in the oxide layer types in the composite and unreinforced samples resulted in a higher wear resistance in the composite samples. Since the wear rate was low during the oxidative wear, this mechanism was considered as mild wear that could be dependant on the thickness of the oxide layer. The SEM micrographs showed bright regions on the surface, which were fully covered by an oxide layer. The EDS results in Fig. 10 II demonstrate the strong peaks of oxygen and magnesium. Mild wear conditions resulted from the
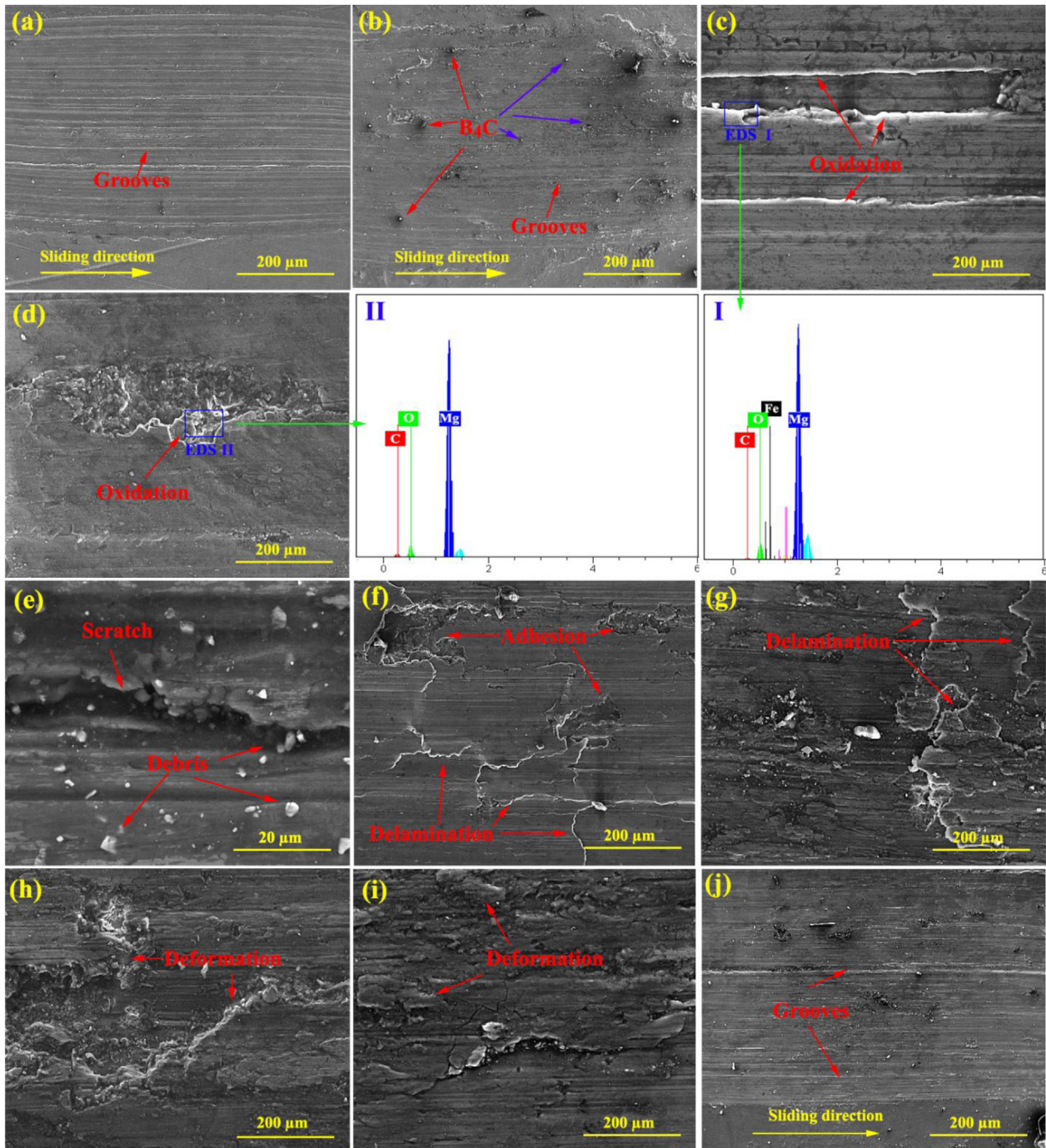
Fig. 10. SEM micrographs and EDS analyses of the worn surfaces of samples with different B_4C contents at various wear conditions: (a) unreinforced alloy at 0.1 m/s under 10 N, (b) 10% B_4C/AZ31 at 0.1 m/s under 10 N, (c) unreinforced alloy at 1 m/s under 10 N, (d) and (e) 10% B_4C/AZ31 at 1 m/s under 10 N, (f) unreinforced alloy at 0.1 m/s under 80 N, (g) 10% B_4C/AZ31 at 0.1 m/s under 80 N, (h) unreinforced alloy at 1 m/s under 80 N, (i) 5% B_4C/AZ31 at 1 m/s under 80 N, and (j) 10% B_4C/AZ31 at 1 m/s under 80 N.

protection of the sliding surface by a thick oxide layer that caused low wear rates [57]. Lim and Ashbay [58] suggested that a threshold velocity must be maintained until the surface heat generated a proper protective oxide film. Moreover, they stated that to maintain the protective film, the exposed sample must provide adequate physical support and oxidative wear was the dominant mechanism for narrow ranges of load

and speed, where the oxidation layer was removed under severe conditions. Unlike the stated results of Lim and Ashby [58], the oxide layers were wider in the present investigation.

Fig. 10f demonstrates the worn surface of the unreinforced sample under the load of 80 N and speed of 0.1 m/s, which represents the delamination mechanism. When delamination is the dominant mechanism, the worn surface is detached in the

form of layers. This is caused by the nucleation of cracks perpendicular to the sliding direction and growth of subsurface cracks during the wear process that leads to the delamination. The propagation of the subsurface cracks shears the surface, which results in the removal of flakes and laminates by coalescence of the cavities and formation of tunnels underneath the worn surface [49]. It was observed that the detachment of flakes formed cracks perpendicular to the sliding direction. The dimensions of the laminates varied from 50 to 300 nm. Severe deformation of the flaky wear debris left shallow cavities on the surface (Fig. 10f). As it was apparent, the width of the formed grooves varied from 20 up to 200 μm.

For sample 10 wt.% $B_4C/AZ31$, numerous flakes and chips were observed on the surface (Fig. 10g). The induced fatigue during the sliding resulted in the deformation of the subsurface, nucleation of cracks, and crack propagation. In fact, the elevation of the applied load promoted the process and led to delamination wear. For all composite samples, it was determined that under high loadings (40–80 N) and low speeds (0.1–0.3 m/s), the delamination occurred simultaneously with an abrasion mechanism. However, this loading range was narrower for sample 20 wt.% $B_4C/AZ31$ (at the speeds of 0.1 and 0.5 m/s and loadings of 60–80 N). The ceramic/matrix interface contributed to void nucleation by providing preferential paths for crack propagation [59]. In addition, it was found that in comparison with the unreinforced alloy, the wear rate of the composite samples at the sliding speed of 0.1 m/s and loading of 80 N was higher. This discrepancy indicated that in the composites, the dominant wear mechanism changed from abrasion to delamination wear. This finding was consistent with earlier previous studies [18,31], which reported the destructive effect of particulate reinforcement on strength in the delamination mechanism. Fig. 10g demonstrates the delamination of composite samples, which represents mild wear conditions. Under constant loading conditions, a transition from abrasion to delamination mechanism was detected in the wear behaviour. The most important factor, which determined the wear mechanism was the temperature elevation of the contact surfaces. Indeed, the increase in temperature led to softening and adhesion of the surface roughness. On the other hand, no adhesion was observed on the counterface. For this reason, the abrasive debris accumulated on the contact surface during the continuous sliding, which resulted in crack nucleation beneath the surface and separation of the laminates [40,49]. After the delamination, the surface was oxidized due to the exposure of the fresh surface to the atmosphere.

Fig. 10h shows that the dominant wear mechanism at high speeds and loadings is plastic deformation for the unreinforced sample. This finding was in agreement with previous reports on other Mg alloys [49]. In these circumstances, local melting of low-melting-temperature phases of the matrix and/or severe plastic deformation induced by thermal softening could occur. According to this figure, the oxides and grooves caused by the abrasion mechanism could not be observed because of the severe surface deformation. Another evidence to confirm the dominant mechanism (plastic deformation) was the small amount of detached debris. In fact, during the plastic deformation, high loadings and sliding speeds enhance the temperature of the sample and the pin, which leads to the melting of the Mg alloy matrix [33].

On the other hand, as shown in Fig. 10i, the deformation extensively damages the surface under the loading conditions for 5 wt.% $B_4C/AZ31$ sample. This damage demonstrates that the transition from the delamination to the plastic deformation wear mechanism occurred by increasing the sliding speed under high loadings. This transition (mild to severe wear) took place mainly owing to the increase in surface roughness, while the reason for the plastic deformation was temperature elevation at the steel counterface/sample interface [60]. With the temperature elevation, the strength of the samples was declined, and consequently, the surface was more susceptible to plastic deformation [33].

The wear rate of the 10 wt.% $B_4C/AZ31$ composite showed that the B_4C particles in the Mg alloys were beneficial to wear resistance. The presence of particles with bimodal distribution in the Mg matrix prevented the thermal softening of the composite. In fact, the presence of B_4C particles and precipitations caused the formation of geometrically necessary dislocations in the matrix during the cooling stage of the casting and ageing process. Consequently, it improved the strength, which resulted in the reduction of the plastic deformation during the wear test (Fig. 10j). Furthermore, it can be said that the presence of ceramic particles hindered the effect of the temperature elevation on the wear mechanism during the test. Additionally, no crack, which could be nucleated due to the loading force, was evident. It can be concluded that the composites strengthened by B_4C particles exhibit higher delamination resistance.

Fig. 11 indicates that at high speeds and loadings, the dominant wear mechanism is abrasion for the 20 wt.% $B_4C/AZ31$ composite. Hence, the wear rate of 20 wt.% $B_4C/AZ31$ composite was higher than that of the unreinforced alloy under the most severe conditions. In these conditions, the wear resistance of this composite sample was not improved. This could be described by the high ductility of the unreinforced AZ31 alloys. Since a broad area of the surface was worn without cracks, the plastic deformation was considered as a severe wear mechanism. Achieving a homogeneous distribution of the particles during the preparation was desirable for obtaining high wear resistance. Nevertheless, a few reinforcement particles agglomerated in the matrix, which was attributed to the abrasive wear mechanism. In this mechanism, due to wedging and ploughing of the steel pin, fine particles were formed, or the debris were removed from the surface, and the particles adhered to the contact surface [40,61]. Wider grooves and scratches could be intensified by abrading using low hardness materials. The grooves were evident at the centre of the abrasive wear area (Fig. 11b). Generally, when a hard material slides over a soft surface, the surface roughness acts as an abrader, and the process is called two-body abrasion. But, when particles, which are sufficiently hard to abrade one or both surfaces, are trapped between the contact surfaces, the phenomenon is called three-body abrasion. This wear mechanism can be active at wear loading condi-
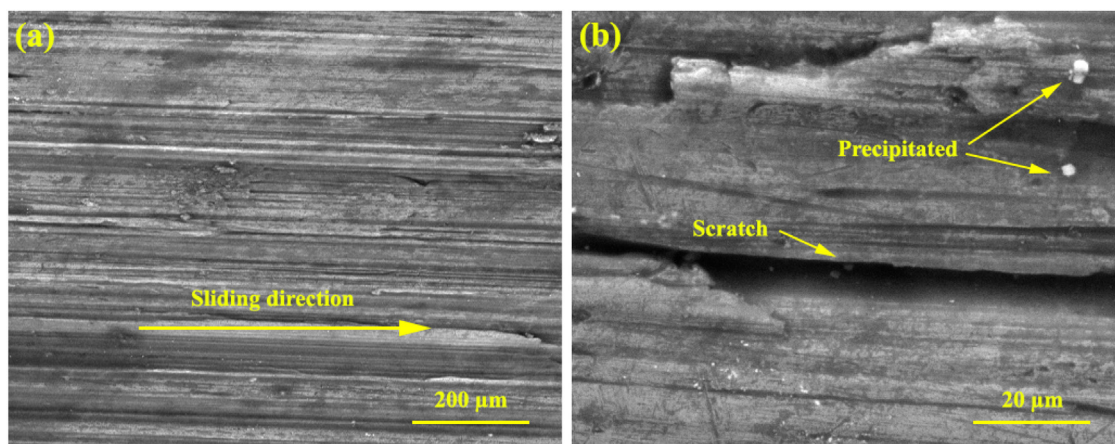
Fig. 11. SEM micrographs of the worn surfaces of 20% B$_4$C/AZ31 sample with different magnifications.

tions and can occur simultaneously with other mechanisms [62,63]. This behaviour can be attributed to the entrapment of the separated and fractured ceramic particles at the sliding interface, which contributes to the abrasive wear. This is consistent with the reports of Kwok and Lim [64] for Al/SiC composites. The presence of debris particles with elongated form in Fig. 10c, confirmed the domination of the abrasion wear mechanism.

By evaluating the parameters of wear rate, friction coefficient and observing the SEM micrographs of the worn surfaces, the wear mechanism maps were constructed for each sample (Fig. 12). As can be seen in the figure, the dominant mechanism in each region is defined, and the boundaries represent the transitions. Thus, regardless of the low sliding speed and low loadings, abrasive wear was the dominant mechanism for all the samples. Nevertheless, an increase in the applied load resulted in the domination of oxidative wear. At low-speed regimes, by increasing the loading, fatigue-induced surficial cracks and separated or delaminated the material; therefore, the wear rate increased and caused a transition from abrasive wear to delamination mechanism. For the unreinforced alloy, this transition occurred at loadings higher than 80 N. But in the composites, higher speeds and loadings were required for shifting the mechanism to the delamination wear. For the 5 wt.% B$_4$C/AZ31 composite, it was revealed that at low sliding speeds, the transition occurred at loadings higher than 150 N. As a matter of fact, when the B$_4$C content was increased to 10 wt.% in the composite, an increase in both sliding speed and the loading was necessary for the transition. It should be noted that, under high loadings; (i) the oxide layer was formed on the surface of the composites, acting as a protecting layer and hindering the transition from the oxidative and abrasive wear to delamination mechanism, and (ii) the B$_4$C particles successfully improved the mechanical properties of the Mg alloy matrix.

Additionally, high B$_4$C contents in the composite (10 wt.% B$_4$C/AZ31) led to the formation of a more compact oxide layer, protecting the surface from metallic wear up to 80 N at low speeds. Thus, higher speeds were required to change the wear mechanism, where delamination was the dominant wear mechanism for the composites and the unreinforced alloy (Fig. 12c). The wear rates of the composite samples were generally lower than that of the unreinforced alloy. The elevated wear rates were observed in Fig. 2c and Fig. 2d for the composites when the loading was more than 80 N at the sliding speeds of 0.5 m/s and 1 m/s, respectively. A gradual transition from delamination to plastic deformation occurred for the composite samples under these intense conditions.

To evaluate the effect of the microstructure on the wear behaviour of the unreinforced alloy, the obtained wear mechanism map was compared with the results of Chen et al. [34] for a dendritic AZ91 Mg alloy under similar loading and speed ranges. They also described two different wear behaviours for the samples; mild wear behaviour, characterized by oxidative and delamination mechanisms, and severe wear behaviour, which was identified by plastic deformation. They constructed a wear transition map, which was consistent with the attained results of this study on AZ91 alloy. This confirmed that the wear parameters had a stronger influence on the wear behaviour in comparison with the microstructure that might be owing to the role of the B$_4$C/matrix interface that could facilitate the nucleation and propagation of cracks.

4. Conclusions

In this investigation, unreinforced AZ31 Mg alloy and AZ31 matrix composites reinforced by bimodal size B$_4$C particles were prepared using a stir casting technique followed by precipitation hardening treatment. Thereafter, the effect of B$_4$C content on the microhardness, dry sliding wear behaviour, and microstructure of the samples was studied. Based on the results, the following conclusions can be drawn:

1. Uniform dispersion of bimodal size B$_4$C particles in the AZ31 matrix can be successfully obtained via the stir casting method. The porosity of the B$_4$C/AZ31 composites was slightly increased by enhancing the B$_4$C content.
2. The Microhardness of the composites was increased by enhancing the B$_4$C content for all the samples. After 10 h of age hardening, the hardness of all composites was in-
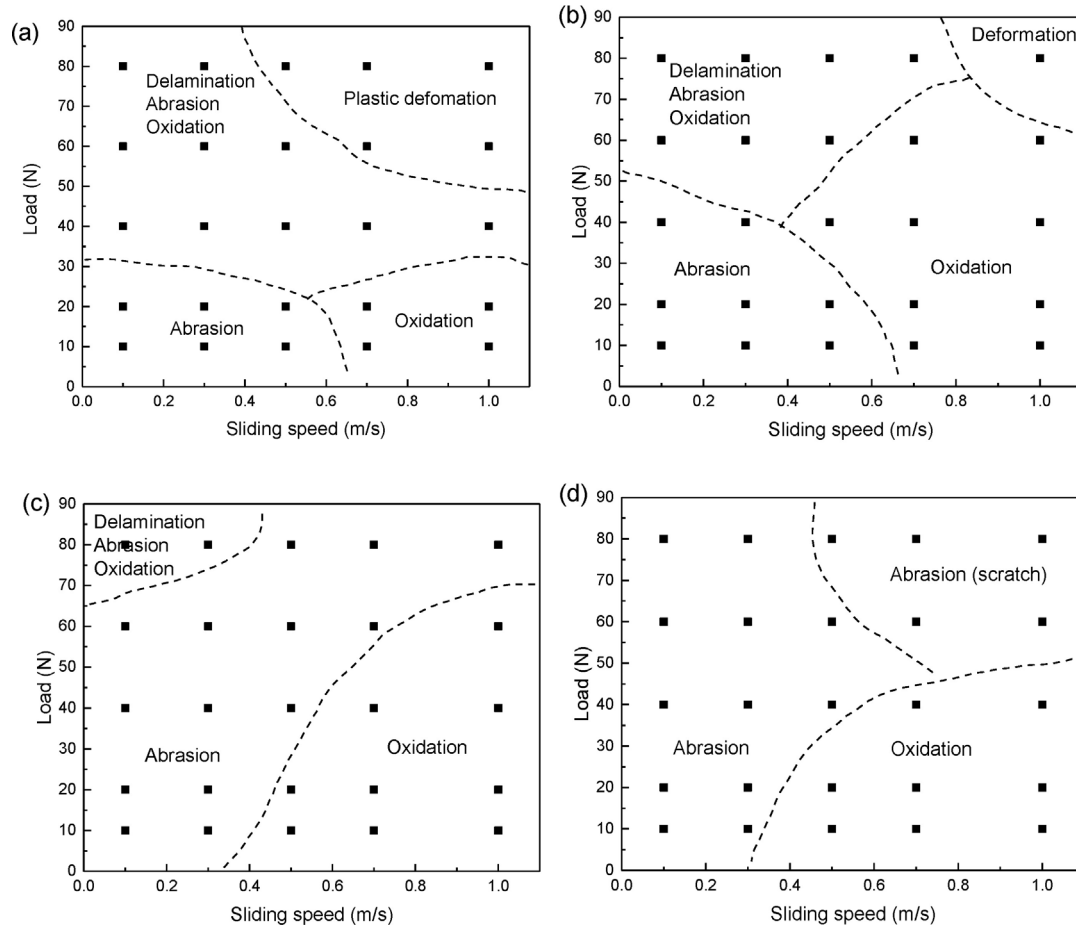
ARTICLE IN PRESS

JID: JMAA
[m5+;July 26, 2021;4:38]

S.K. Moheimani, A. Keshtgar, S. Khademzadeh et al.
Journal of Magnesium and Alloys xxx (xxxx) xxx

Fig. 12. Wear mechanism maps for samples with different B$_4$C contents: (a) unreinforced alloy, (b) 5% B$_4$C/AZ31, (c) 10% B$_4$C/AZ31, and (d) 20% B$_4$C/AZ31.

creased as a consequence of the homogeneous distribution of the reinforcement particles.

3. The addition of B$_4$C particles to the AZ31 matrix caused a considerable decrease in the wear rate.

4. The oxidative wear mechanism was dominant at low loadings (10–40 N) and high speeds. Oxidative wear was observed more frequently for the composite samples, which had a protective oxide layer and a minimum wear rate of 0.013 mm^3/Nm for sample 10 wt.% B$_4$C.

5. The lowest coefficient of friction (0.3) was observed for the composite samples for 10 wt.% B$_4$C at the speed of 1 m/s.

6. By increasing the load, the plastic deformation was dominant due to the elevation of the frictional heating that resulted in the surface melting.

7. At low speeds and under low loadings, the abrasive wear was dominant, while by increasing the load, delamination was dominant. This behaviour was similar to that of AZ31 alloys and implied the insignificant effect of microstructure on the wear conditions.

8. A delay was detected for the transition to delamination wear mechanism when the B$_4$C content was increased (sample 10 wt.% B$_4$C/AZ31).

9. Under the most intense conditions (sliding speed of 0.5–1 m/s and loadings of 60–80 N), the dominant mechanism was abrasive wear for the sample containing 20 wt% B$_4$C.

All in all, it can be concluded that under these circumstances, the presence of B$_4$C particles did not improve the wear resistance of composite samples.

Declaration of Competing Interest

The authors declare that they have no known competing financial interests or personal relationships that could have appeared to influence the work reported in this paper.

References

[1] M. Tayebi, S. Nategh, H. Najafi, A. Khodabandeh, J. Alloys Compd. 830 (2020) 154709.

[2] M. Tayebi, H. Najafi, S. Nategh, A. Khodabandeh, Met. Mater. Int. (2020).

[3] A. Saboori, E. Padovano, M. Pavese, C. Badini, Mater 11 (1) (2018).

[4] D. Rahmatabadi, M. Tayyebi, N. Najafizadeh, R. Hashemi, M. Rajabi, Mater. Sci. Technol. 37 (1) (2021) 78–85.

[5] H. Sharifi, K. Ostovan, M. Tayebi, A. Rajaee, Tribol. Int. 116 (2017) 244–255.

[6] F. Jafari, H. Sharifi, M.R. Saeri, M. Tayebi, Silicon 10 (2018) 2473–2481.

[7] H. Sharifi, M. Tayebi, M. Honarmand, Mater. Res. Express 3 (10) (2016).

[8] H. Sharifi, V. Eidivandi, M. Tayebi, A. Khezrloo, E. Aghaie, Heat Mass Transf. und Stoffuebertragung 53 (12) (2017) 3621–3627.

[9] H.M.H.M. Soltani, M. Tayebi, Int. J. Refract. Met. Hard Mater. 87 (2020) 105172.

[10] H.G. Adivi, I. Ebrahimzadeh, M. Hadi, M. Tayebi, Surf. Rev. Lett. 27 (11) (2020) 2050004.

[11] S.K. Moheimani, M. Dadkhah, M.H. Mosallanejad, A. Saboori, Met. 11 (1) (2021).

[12] T.R. Prabhu, Tribol. - Mater. Surfaces Interfaces 10 (4) (2016) 163–171.

[13] K. Deng, J. Shi, C. Wang, X. Wang, Y. Wu, K. Nie, K. Wu, Compos. Part A Appl. Sci. Manuf. 43 (8) (2012) 1280–1284.

[14] M. Tayebi, D. Bizari, Z. Hassanzade, Mater. Sci. Eng. C 113 (2020) 110974.

[15] S. Elahinejad, H. Sharifi, M. Tayebi, A. Rajaee, Mater. Res. Express 4 (11) (2017).

[16] M. Tayebi, M. Jozdani, M. Mirhadi, J. Alloys Compd. 809 (2019) 151753.

[17] M.S. Bayati, H. Sharifi, M. Tayebi, T. Isfahani, Mater. Res. Express 6 (10) (2019).

[18] M. Paidar, O.O. Ojo, H.R. Ezatpour, A. Heidarzadeh, Surf. Coatings Technol. 361 (2019) 159–169.

[19] S.J. Huang, A. Abbas, B. Ballóková, J. Mater. Res. Technol. 8 (5) (2019) 4273–4286.

[20] Y. Yao, L. Chen, J. Mater. Sci. Technol. 30 (7) (2014) 661–665.

[21] J. Zhu, J. Qi, D. Guan, L. Ma, R. Dwyer-Joyce, Tribol. Int. 146 (2020) 106253.

[22] A. Kumar, P.M. Pandey, J. Magnes. Alloy. 8 (3) (2020) 883–898.

[23] M. Godzierz, A. Olszówka-Myalska, N. Sobczak, R. Nowak, P. Wrześniowski, J. Magnes. Alloy. (2020).

[24] S. Paulo Hang Jutanaiman, A. Zulfia Syahrial, IOP Conf. Ser. Mater. Sci. Eng. 924 (2020) 12020.

[25] A. Singh, N. Bala, Metall. Mater. Trans. A 48 (2017).

[26] L.F. Guleryuz, S. Ozan, D. Uzunsoy, R. Ipek, Powder Metall. Met. Ceram. 51 (7) (2012) 456–462.

[27] G.H. Majzoobi, K. Rahmani, Int. J. Miner. Metall. Mater. 27 (2) (2020) 252–263.

[28] Q.C. Jiang, H.Y. Wang, B.X. Ma, Y. Wang, F. Zhao, J. Alloys Compd. 386 (1) (2005) 177–181.

[29] V. Kevorkijan, S. Davor Škapin, Mater. Manuf. Process. 24 (12) (2009) 1337–1340.

[30] E. Ghasali, M. Alizadeh, M. Niazmand, T. Ebadzadeh, J. Alloys Compd. 697 (2017) 200–207.

[31] H. Somekawa, S. Maeda, T. Hirayama, T. Matsuoka, T. Inoue, T. Mukai, Mater. Sci. Eng. A 561 (2013) 371–377.

[32] P. Bala Srinivasan, J. Liang, C. Blawert, W. Dietzel, Appl. Surf. Sci. 256 (10) (2010) 3265–3273.

[33] C.Y.H. Lim, S.C. Lim, M. Gupta, Wear 255 (1) (2003) 629–637.

[34] H. Chen, A.T. Alpas, Wear 246 (1) (2000) 106–116.

[35] S.Q. Wang, Z.R. Yang, Y.T. Zhao, M.X. Wei, Tribol. Lett. 38 (1) (2010) 39–45.

[36] C. Taltavull, B. Torres, A.J. López, J. Rams, Wear 301 (1) (2013) 615–625.

[37] A. Zafari, H.M. Ghasemi, R. Mahmudi, Wear 292–293 (2012) 33–40.

[38] M. Habibnejad-Korayem, R. Mahmudi, H.M. Ghasemi, W.J. Poole, Wear 268 (3) (2010) 405–412.

[39] J.F. Archard, J. Appl. Phys. 24 (8) (1953) 981–988.

[40] A. Abbas, S.J. Huang, B. Ballóková, K. Sülleiová, Tribol. Int. 142 (2020) 105982.

[41] J. Singh, Friction 4 (3) (2016) 191–207.

[42] M. Tayebi, M. Jozdani, M. Mirhadi, J. Alloys Compd. 809 (2019).

[43] R.J. Arsenault, N. Shi, C.R. Feng, L. Wang, Mater. Sci. Eng. A 131 (1) (1991) 55–68.

[44] M. Tayebi, M. Tayebi, M. Rajaee, V. Ghafarnia, A.M. Rizi, J. Alloys Compd. 853 (2021) 156794.

[45] O.S. Salih, H. Ou, X. Wei, W. Sun, Mater. Sci. Eng. A 742 (2019) 78–88.

[46] S.-J. Huang, A.N. Ali, Mater. Sci. Eng. A 711 (2018) 670–682.

[47] Y. Jin, K. Wang, W. Wang, P. Peng, S. Zhou, L. Huang, T. Yang, K. Qiao, B. Zhang, J. Cai, Hailiang Yu, Mater. Charact. 150 (2019) 52–61.

[48] H. Yu, Y. Xin, M. Wang, Q. Liu, J. Mater. Sci. Technol. 34 (2) (2018) 248–256.

[49] S. García-Rodríguez, B. Torres, A. Maroto, A.J. López, E. Otero, J. Rams, Wear 390–391 (2017) 1–10.

[50] X. Du, E. Zhang, Mater. Lett. 61 (11) (2007) 2333–2337.

[51] M. Esmaily, N. Mortazavi, J.E. Svensson, M. Halvarsson, A.E.W. Jarfors, M. Wessén, R. Arrabal, L.G. Johansson, Mater. Chem. Phys. 180 (2016) 29–37.

[52] J. Jayaraman, R. Kuppusamy, H. Rao, Sci. Eng. Compos. Mater. 23 (1) (2016) 61–66.

[53] E. Aghaie, A. Najafi, H. Maleki-Ghaleh, H. Mohebi, Surf. Eng. 29 (3) (2013) 177–182.

[54] M. Ramezani, Z.M. Ripin, Int. J. Adv. Manuf. Technol. 51 (1) (2010) 93–102.

[55] Soorya Prakash, Balasundar K., Nagaraja P., Gopal S., P. M., V. Kavimani, J. Magnes. Alloy. 4 (3) (2016) 197–206.

[56] M.J. Neale, Butterworth-Heinemann, 1995.

[57] J. Wu, X. Zeng, L. Luo, Q. Yuan, Mater. Mech. Eng. 11 (2015) 25.

[58] S.C. Lim, M.F. Ashby, Acta Metall. 35 (1) (1987) 1–24.

[59] J. Zhang, A.T. Alpas, Mater. Sci. Eng. A 160 (1) (1993) 25–35.

[60] J. Zhang, A.T. Alpas, Acta Mater. 45 (2) (1997) 513–528.

[61] C. Taltavull, P. Rodrigo, B. Torres, A.J. López, J. Rams, Mater. Des. 56 (2014) 549–556.

[62] M. Jamshidijam, A. Akbari-Fakhrabadi, S.M. Masoudpanah, G.H. Hasani, R.V. Mangalaraja, Tribol. Trans. 56 (5) (2013) 827–832.

[63] M. Zhou, X. Qu, L. Ren, L. Fan, Y. Zhang, Y. Guo, G. Quan, Q. Tang, B. Liu, H. Sun, Mater 10 (12) (2017).

[64] J.K.M. Kwok, S.C. Lim, Compos. Sci. Technol. 59 (1) (1999) 65–75.